



Publication Year	2018
Acceptance in OA@INAF	2020-12-17T17:52:56Z
Title	Röntgen spheres around active stars
Authors	Locci, Daniele; CECCHI PESTELLINI, Cesare; MICELA, Giuseppina; CIARAVELLA, Angela; ARESU, Giambattista
DOI	10.1093/mnras/stx2370
Handle	http://hdl.handle.net/20.500.12386/28958
Journal	MONTHLY NOTICES OF THE ROYAL ASTRONOMICAL SOCIETY
Number	473

Röntgen spheres around active stars

Daniele Locci,^{1,2} Cesare Cecchi-Pestellini,^{2★} Giuseppina Micela,²
Angela Ciaravella² and Giambattista Aresu³

¹*Dipartimento di Fisica e Chimica, Università di Palermo, P.zza del Parlamento 1, I-90134, Italy*

²*INAF – Osservatorio Astronomico di Palermo, P.zza del Parlamento 1, I-90134 Palermo, Italy*

³*INAF – Osservatorio Astronomico di Cagliari, Via della Scienza 5, I-09047 Selargius, Italy*

Accepted 2017 September 8. Received 2017 September 8; in original form 2017 April 16

ABSTRACT

X-rays are an important ingredient of the radiation environment of a variety of stars of different spectral types and age. We have modelled the X-ray transfer and energy deposition into a gas with solar composition, through an accurate description of the electron cascade following the history of the primary photoelectron energy deposition. We test and validate this description studying the possible formation of regions in which X-rays are the major ionization channel. Such regions, called Röntgen spheres may have considerable importance in the chemical and physical evolution of the gas embedding the emitting star. Around massive stars the concept of Röntgen sphere appears to be of limited use, as the formation of extended volumes with relevant levels of ionization is efficient just in a narrow range of gas volume densities. In clouds embedding low-mass pre-main-sequence stars significant volumes of gas are affected by ionization levels exceeding largely the cosmic-ray background ionization. In clusters arising in regions of vigorous star formation X-rays create an ionization network pervading densely the interstellar medium, and providing a natural feedback mechanism, which may affect planet and star formation processes.

Key words: atomic processes – radiative transfer – X-rays: ISM – X-rays: stars.

1 INTRODUCTION

The understanding of physical processes in the circumstellar environment of protostars and young stars provides crucial information on how discs and planets form and survive (e.g. Williams & Viti 2014). These processes and star formation itself are regulated by a variety of feedback mechanisms, such as direct and dust reprocessed radiation pressure, photoionization flows, stellar wind and supernova explosions. The response of gas gives rise to complicated chemistry and dynamics, as well as radiation fields, which, in turn, perturb the behaviour of the molecular gas, affecting the chemistry (e.g. Bradford et al. 2011), and impacting the efficiency of star formation (e.g. Dale & Bonnell 2011). Since a tremendous number of stars at all ages are observed to be X-ray emitters in nearby star-forming regions (Feigelson 2010), an important question is whether and how X-ray radiation participates in the process of star, disc and planet formation and in their evolution. Although X-ray luminosities are relatively small fractions of the bolometric luminosity, such radiation effectively penetrates and ionizes otherwise neutral molecular gases and may even melt solid dust particles.

X-ray emission has been detected in the most massive Wolf-Rayet and OB stars as well as in low-mass M dwarf stars, in compact objects and even in some sub-stellar mass brown dwarfs. X-ray luminosities range from 10^{25} up to 10^{35} erg s⁻¹ (e.g. in Eta Carina, Hamaguchi et al. 2014). In low-mass stars X-ray emission is produced by the violent heating of the stellar corona through magnetic dynamo and magnetic reconnection, while in high-mass O and early B-type stars are supersonic shocks in the stellar winds to generate X-rays on both stellar and parsec scales. In young solar-like stars, X-ray flares with luminosities orders of magnitude more powerful than seen in the contemporary Sun are frequently observed.

In fact, studies of stellar proxies for the Sun have shown that young solar-type stars emit X-rays at a level three to four orders of magnitude higher than the present-day Sun, both during the pre-main-sequence (PMS) phase when the emission is dominated by intense daily or weekly flares (Favata et al. 2005), and during the first phases of the main sequence. From studies of stellar proxies for the Sun (e.g. Ribas et al. 2005), it appears that for a 100 Myr star the integrated fluxes in the extreme ultraviolet are lower than X-rays. The ratio of these fluxes remains within a factor of 2 for stars as old as 1 Gyr, while in the Sun is about 4. Moreover, the star luminosity seems to be characterized by evolutionary time-scales that are different in different spectral bands (Micela 2002). The

* E-mail: cecchi-pestellini@astropa.unipa.it

X-ray luminosity evolution of M stars is slower than that of G stars, and may present frequent flaring activity. Even if the ratio between X-ray and bolometric luminosities is typically larger in M stars than in solar-type stars, the absolute value of the X-ray luminosity is lower at each age.

The effects of X-rays can be wide ranging or relatively local. Soft X-rays are absorbed closer to the source than X-rays with energy greater than 1 keV. The absorption cross-section of hard X-rays are generally very small, so that such radiation may affect a whole galaxy to some extent. The interaction of X-rays with gas clouds has been widely studied in the literature. The first detailed studies of X-ray illuminated regions were performed by Tarter et al. (1969) and Tarter & Salpeter (1969) for optically thin and thick media, respectively. These authors assumed the spectral shape of thermal bremsstrahlung. It soon became apparent that high-energy flat spectra would induce ionization profiles significantly smoother than the sharp boundary between H II and H I regions (Strömgren sphere) produced by standard stellar blackbody-like emission (see Bahcall, Bahcall & Kozlovsky 1971). Since then, following the opening of the X-ray Universe the modelling of regions exposed to X-rays was extended to molecular gas in a variety of sources such as active galactic nuclei, and molecular clouds with embedded among others massive and PMS stars (e.g. Maloney et al. 1996). Depending on specific effects X-ray illuminated regions have been termed X-ray dominated regions when the thermochemical balance of the gas is involved (e.g. Tiné et al. 1997) or Röntgen spheres (Lorenzani & Palla 2001) to indicate the extent of the X-ray ‘sphere of influence’ on the ionization balance around a source.

As most star formation in our galaxy occurs within embedded clusters, the radiative and mechanical energy injections produced by cluster members can shape the background environment and thereby provide a feedback mechanism. There is now a wealth of information on embedded clusters coming from multiwavelength observations, such as far- and extreme-ultraviolet (Hollernbach & Gorti 2009; Holden et al. 2011) and X-rays (Adams, Fatuzzo & Holden 2012). In the first case a significant fraction of the luminosity is produced by the most massive members of the cluster (e.g. Fatuzzo & Adams 2008), while in the X-ray band the total luminosity may be globally contributed by the totality of stars. Frequently, background radiation fields in the ultraviolet can dominate even locally, leading as a result to the evaporation of circumstellar discs, thus decreasing the planet-forming rate within a cluster. In contrast, mass-loss due to X-rays is dominated by the radiation flux from the central star, with the exception of the outer regions in geometrically thin and optically thick discs where background cluster dominates (see Adams et al. 2012). In addition there is a diffuse background ionization level generally exceeding the one generated by cosmic-ray energy deposition (Lorenzani & Palla 2001). These elevated ionization rates deriving from the merging of individual Röntgen spheres, suggest that X-rays can affect ionization, chemistry and heating in the material between young stellar objects.

In this work, we study the X-ray environment of stars of different spectral types and age either isolated and clustered. We consider two representative environments, the Cygnus OB2 association among the most massive clusters in our Galaxy, and the Orion Nebula Cluster (ONC) that was the first cluster of PMS stars to be detected in the X-ray band (Giacconi et al. 1972). The *Chandra Orion Ultradeep Project* (COUP; Getman et al. 2005) has shown that ONC contains more than 1600 X-ray sources, approximately 1400 of which are young stellar objects.

In the next section, we solve the appropriate radiative transfer problem, and we derive formulae for the ionization rates considering

photoionization, the Auger effect and the production of secondary electrons through electronic impacts. In Section 3, we revise the concept of Röntgen sphere, while in Section 4, we modify the description of the ionization balance in circumstellar regions allowing for the presence of stellar ultraviolet irradiation. Results for massive stars are reported in Section 5, while an analysis of the effects on circumstellar gas around low-mass stars is in Section 6. Finally, last Section contains our conclusions.

2 X-RAY TRANSFER AND ENERGY DEPOSITION

X-rays impinging upon a cloud of gas and dust of solar-like composition photoionizes the gas producing a flux of high-energy photoelectrons, which deposit their energy into the gas, and to some extent in the interior of dust particles. In a partially neutral medium, electrons ionize, excite and dissociate atomic and molecular species, as well as heat the gas through Coulomb collisions. Such energy deposition events may be estimated considering all the possible degradation histories of the energetic electron cascade. The derived yields allow us to determine the ionization, dissociation, excitation and heating rates throughout the illuminated region (Dalgarno, Yan & Liu 1999).

2.1 Radiative transfer

We consider 1D geometry in which a stratified cloud consisting of gas and dust is illuminated by a radially incident X-ray photon flux. This flux at distance r from the stellar source is given by the solution to the radiative transfer problem

$$\mathcal{F}_X(E, r) = \frac{\mathcal{L}_X(E)}{4\pi r^2} \times e^{-\tau(E, r)}, \quad (1)$$

where \mathcal{L}_X is the stellar X-ray spectral luminosity (in $\text{ergs s}^{-1} \text{eV}^{-1}$) and $\tau(E, r)$ is the optical depth that depends on the total photoionization cross-section.

We adopt radiative photoionization cross-sections of individual elements ($Z \leq 30$) and their ions computed by Verner & Yakovlev (1995). In the case of molecular hydrogen, we fit the laboratory measurements reported in Samson & Haddad (1994), while for H_2^+ we adopt the calculations by Morita & Yabushita (2008). For heavy elements bound in molecules or molecular ions, the X-ray absorption cross-sections can be obtained approximately by adding the atomic cross-sections. As far as the computation of the photoelectric cross-section is concerned we may simply construct the total cross-section by weighting the individual cross-sections σ_k with element abundances, Y_k , subtracted by the fractions of those elements locked into dust, δ_k

$$\sigma_{\text{h}}^{(\oplus)}(E) = \sum_k Y_k (1 - \delta_k) \sigma_k(E), \quad (2)$$

where

$$\sigma_k(E) = \sum_i \sigma_{k,i}(E) \quad (3)$$

is the sum of the contributions of the various shells in the atoms. In computing $\sigma_k(E)$, we should take into account that the k -th element is in various ionization stages. In practice we consider only neutral atoms, and at most double-charged ions because highly charged ions undergo fast charge exchange reactions

$$Y_k \sigma_{k,i}(E) = Y_{k^0} \sigma_{k^0,i}(E) + Y_{k^+} \sigma_{k^+,i}(E) + Y_{k^{2+}} \sigma_{k^{2+},i}(E) \quad (4)$$

with $Y_k = Y_{k^0} + Y_{k^+} + Y_{k^{2+}}$. Heavy elements composing dust grains provide a similar contribution

$$\sigma_{\text{h}}^{(\text{d})}(E) = \sum_k Y_k \delta_k \sigma_k(E). \quad (5)$$

To the aim of computing the optical depth the separation in gas- and solid-phase elements is immaterial, while it is not for the calculation of the total ionization rate, because a fraction of the electrons is not ejected into the gas-phase after being released in the interior of a dust grain (see Section 2.2).

For $E \gtrsim 5$ keV, Compton ionization is more efficient than photoionization (Yan, Sadeghpour & Dalgarno 1998). Unlike photoionization or fast charged particle scattering, total cross-sections for single ionization via Compton scattering (also termed incoherent scattering) are usually largely independent of atomic properties, such as geometric sizes of atoms and electron correlation. In Compton ionization, the photon is not absorbed but scattered, and it shares energy and momentum with the ejected electron. At high energies the binding energies of electrons in atoms or molecules can be ignored, and the cross-sections are those for scattering by free electrons. For energies higher than 1 keV the incoherent cross-section for atomic hydrogen is approximately the same as the free electron Klein–Nishina cross-section, σ_{KN} . Moreover, scattering cross-sections are very small, in fact, of the order of the electron Thomson scattering cross-section, σ_{Th} ($\sim 1 \text{ b} = 10^{-24} \text{ cm}^2$). Thus, in the computation of the optical depth we use for all species the Klein–Nishina scattering formula (Rybicki & Lightman 2004) in the non-relativistic regime ($E \ll mc^2$)

$$\sigma_{\text{C}}(E) = \mathcal{Z} \times \sigma_{\text{Th}} \left[1 - \frac{E}{mc^2} + \frac{26}{5} \left(\frac{E}{mc^2} \right)^2 \right] = \mathcal{Z} \times \sigma_{\text{KN}}, \quad (6)$$

where

$$\mathcal{Z} = 1 + 2Y_{\text{He}} + \sum_k Z_k Y_k \quad (7)$$

Y_{He} being the fractional total helium concentration and Z_k is the number of electrons in the k -th species. In equation (7), we implicitly assume that the incoherent cross-section of molecular hydrogen is twice the one for atomic hydrogen (cf. equation 8), and all the elements are in neutral form. The correct formulation of non-relativistic Compton ionization cross-sections for H, H₂ and He (Jackson 1975) is included in the calculation of the total ionization rate of the gas. Here, we report the expression

$$\sigma_{\text{C}}^{(i)}(E) = \frac{3n_e^{(i)}}{8} \sigma_{\text{Th}} (4/3 + t + t^3/3), \quad (8)$$

where $t = 1 - mc^2/E \times x^{(i)}/(1 - x^{(i)})$, $x^{(i)} = \mathcal{I}^{(i)}/E$. In the previous expression, $i = 1, 2$ and 3 for H, H₂ and He, respectively; $n_e^{(i)}$ is the number of electrons equal to 1, 2 and 2, and $\mathcal{I}^{(i)} = 13.6, 15.4$ and 24.6 eV, the ionization potential. Finally, the cross-section thresholds are 1.87, 1.99 and 2.51 keV.

The energy-dependent optical depth results

$$\tau(E) = \sigma_{\text{T}}(E) N_{\text{H}} = (f_1 \sigma_{\text{H}} + f_2 \sigma_{\text{H}_2} + Y_{\text{He}} \sigma_{\text{He}} + Y_{\text{He}^+} \sigma_{\text{He}^+} + \sigma_{\text{h}} + \sigma_{\text{C}}) \times N_{\text{H}} \quad (9)$$

in which $\sigma_{\text{h}} = \sigma_{\text{h}}^{(\text{g})} + \sigma_{\text{h}}^{(\text{d})}$, N_{H} is the total hydrogen column density and f_1 and f_2 are the fractional abundances of atomic and molecular hydrogen, respectively ($f_1 + 2 \times f_2 \sim 1$).

In Fig. 1, we compare the approximate cross-section given in Lorenzani & Palla (2001)

$$\sigma_{\text{A}}(E) = \bar{\sigma} \times (\nu/\nu_{\text{X}})^{-n} = 2.16 \times 10^{-4} (E/1 \text{ keV})^{-2.51} \text{ Mb} \quad (10)$$

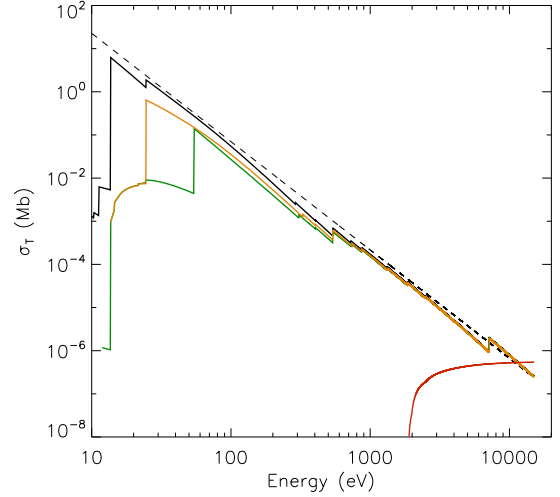


Figure 1. Total photoionization cross-section in Mb ($1 \text{ Mb} = 1 \times 10^{-18} \text{ cm}^2$) as a function of the energy of the incoming photon in eV, for a gas with solar abundances (Asplund et al. 2009). Black solid line: neutrals; yellow line: singly ionized species; and green line: double charged ions. The red solid line represents the Compton ionization cross-section, equation (12), the thin dashed line represents the approximate photoionization cross-section given in Lorenzani & Palla (2001), equation (10).

with our computed σ_{T} in various configurations, and the contribution due to Compton ionization plotted separately. We adopt the solar abundances reported in Asplund et al. (2009), and we set $Y_{\text{He}} = 0.085$.

2.2 X-ray ionization

Primary X-ray ionization is given by the following relation:

$$\mathcal{S}'_{\text{X}} = \sum_k \sum_i \int_{E_{k,i}}^{E_{k,i+1}} \frac{\mathcal{F}_{\text{X}}(E, r)}{E} [Y_k \sigma_{k,i}(E) + \sigma_{\text{C}}(E)] dE, \quad (11)$$

where $E_{k,i}$ is the energy threshold, $i = 1, 2$, and 3 identifies M, L and K shell, respectively, and $E_{k,4} = \infty$. Here, the sum over k includes H, He, He⁺, H₂ and H₂⁺ in addition to heavy elements. Furthermore, the Compton contribution has been modified to incorporate the non-approximate cross-sections given in equation (8)

$$\sigma_{\text{C}} = \sum_{j=1}^3 f_j \sigma_{\text{C}}^{(j)}(E) + (\mathcal{Z} - 1 - 2Y_{\text{He}}) \times \sigma_{\text{KN}}, \quad (12)$$

where $f_3 = Y_{\text{He}}$ is the total helium abundance with respect to hydrogen.

The product of a primary ionization is one fast photoelectron, or more if the Auger effect occurs, that gives rise to a cascade of secondary ionizations. The energy of the fast photoelectron is given by the difference of the energy of the incident photon and the energy threshold $E_{k,i}$ of the ejected electron. The rate of secondary ionization of the k -th element due to photoelectrons is given by the relation

$$\mathcal{S}''_k = \int n_{\text{sec}}(E) v(E) \sigma_k^{(e)}(E) dE \quad (13)$$

(e.g. Adamkovics, Glassgold & Meijerink 2011), where $v(E)$ is the electron speed, $n_{\text{sec}}(E)$ the absolute number distribution of secondary electrons and $\sigma_k^{(e)}$ the electron impact ionization

cross-section. We estimate equation (13) by means of the semi-empirical relation

$$\zeta_k'' = \sum_i \int_{E_{k,i}}^{E_{k,i+1}} \frac{\mathcal{F}_X(E, r)}{E} Y_k \sigma_{k,i}(E) \frac{(E - E_{k,i})}{W} dE \quad (14)$$

with W is the mean energy per ion pair (e.g. Dalgarno et al. 1999), which is the initial energy of the photoelectron divided by the number of secondary ionizations produced as the particle comes to rest. To include Auger ionization, we have to supplement equation (14) with

$$\zeta_k^A = \sum_i \int_{E_{k,i}}^{E_{k,i+1}} \frac{\mathcal{F}_X(E, r)}{E} Y_k \sigma_{k,i}(E) \frac{\mathcal{E}_{k,i}}{W} dE, \quad (15)$$

where $\mathcal{E}_{k,i}$ is the energy of the Auger electron emitted by the i -th shell of the k -th element. However, assuming that the Auger electrons contribute to the ionization with an energy $\mathcal{E}_{k,i}$ comparable with the energy $E_{k,i}$ (Maloney et al. 1996), the total secondary ionization reads as

$$\zeta_X'' = \sum_k \sum_i \int_{E_{k,i}}^{E_{k,i+1}} \mathcal{F}_X(E, r) \left(\frac{Y_k \sigma_{k,i}(E)}{W} \right) dE \quad (16)$$

To take into account heavy elements locked into dust grains, we slightly modify the fraction in the integrand in equation (16) as follows:

$$\frac{Y_k \sigma_{k,i}(E)}{W} \rightarrow \frac{Y_k (1 - \delta_k) \sigma_{k,i}(E)}{W} + \frac{Y_k \delta_k \sigma_{k,i}(E)}{W} \times \frac{H(E - E_g, E_{k,i})}{E}, \quad (17)$$

where E_g is the energy loss within the grain, that depends on the grain size and materials, and $H(x, y) = 0$ when $x \leq y$, and equal to $x (= E - E_g)$ otherwise. We compute E_g using the range of electrons in silicate and carbon materials taken in the NIST *ESTAR* data base.¹

Equation (16) is supplemented by Compton ionization as

$$\zeta_{X,C}'' = \int_{E_i}^{\infty} \frac{\mathcal{F}_X(E, r)}{E} \times \frac{\sigma_C(E) E_C(E)}{W} dE \quad (18)$$

with $E_i = 1.87$ keV, and $E_C(E)$ is the energy of the released Compton electron. In the Compton energy domain an emitted photon will scatter until, in a finite medium it escapes completely. The number of scattering acts is approximately $\mathcal{N}_s \approx \max(\tau_C, \tau_C^2)$ (Rybicki & Lightman 2004) with τ_C the Compton optical depth. The Compton parameter y_C is defined as the number of scattering events times the average fractional change of energy per scattering $y_C \sim \mathcal{N}_s \times (E/mc^2)$. We thus approximate the energy of the released Compton electron as

$$E_C(E) = \begin{cases} y_C E & y_C < 1 \\ E & y_C > 1 \end{cases} \quad (19)$$

For the calculation of secondary ionization, we compute W as a function of the energy of the primary photoelectron for a mixture of H, He and H_2 exploiting the numerical code described in Cecchi-Pestellini, Ciaravella & Micela (2006). We follow the chain of discrete energy deposition events using the method put forward by Cravens, Victor & Dalgarno (1975). We adopt the electron impact cross-sections for excitation, ionization, dissociation and elastic collisions listed in Dalgarno et al. (1999). To include the contribution of the heavy elements that are not traced by equation (16), we rely on an approximate treatment that makes use of the relative rather than

Table 1. Peak electronic ionization cross-sections in Mb.

Element	$\sigma_k^{(e)a}$	R_1^b	R_2^c	R_1^d	R_2^d
H	88.7	1.0			
C	211.3	2.38	0.89	3.4	0.82
N	146.9	1.66	0.84	2.2	0.75
O	143.0	1.61	0.84	2.2	0.67
Ne	73.10	0.82	0.89	1.1	0.48
Na	490.6	5.53	1.29	7.3	0.40
Mg	529.1	5.96	1.36	7.91	0.64
Al	827.1	9.32	1.27		
Si	715.0	8.06	1.66	10.0	2.3
S	541.3	6.10	1.38	6.7	2.1
Cl	420.5	4.74	0.93		
Ar	327.8	3.69	1.05	3.7	1.8
K	852.1	9.6	1.88	13	1.5
Ca	873.3	9.85	1.31		
Fe	494.1	5.57	1.30	8.0	1.6

Notes. ^apeak of the electron impact ionization cross-section for k -th species, Bartlett & Stelbovics (2004); ^b $R_1 = \sigma_k^{(e)}/\sigma_H^{(e)}$, Bartlett & Stelbovics (2004); ^c $R_2 = \sigma_{k^+}^{(e)}/\sigma_H^{(e)}$, this work; and ^dAdamkovics et al. (2011).

the absolute secondary energy distribution (Maloney et al. 1996). Following Adamkovics et al. (2011), we estimate the secondary ionization rates for the individual heavy elements using the ratio of the peaks of the ionization cross-sections for electronic impact $\sigma^{(e)}$

$$\zeta_k'' = \frac{\sigma_k^{(e)}}{\sigma_H^{(e)}} \zeta_X'', \quad (20)$$

where k counts heavy elements and ζ_X'' is the rate given in equation (16). Values of the cross-section ratios for neutral atoms are taken in Bartlett & Stelbovics (2004) and reported in Table 1. Unfortunately, these authors do not include ions. Although double charged atomic ions have, in general, negligible abundances because of rapid charge exchange with atomic and molecular hydrogen and other species, singly ionized atoms may be abundant. We estimate the cross-section ratios for these species exploiting the data reported in Adamkovics et al. (2011), that have been derived using much older data by Tarawa & Kato (1987). We perform a linear fit of the relation between \hat{R}_1 and the geometrical mean $\sqrt{\hat{R}_1 \times R_2}$ in which $R_1 = \sigma_k^{(e)}/\sigma_H^{(e)}$ for neutrals, \hat{R}_1 the normalization to its maximum value and $R_2 = \sigma_{k^+}^{(e)}/\sigma_H^{(e)}$ the ratio for ions. While the overall fit is not particularly good, it is difficult to evaluate the accuracy of the approximate formula, equation (20), in the absence of a direct calculation of the secondary electron distribution.

If the gas has a significant molecular component the previous treatment is invalid. Electron impact ionization cross-sections for simple molecules such as water or carbon monoxide have a threshold around 20 eV, show a broad maximum at approximately 100 eV, and then they decline to reach roughly their values at the threshold around 1 keV (e.g. Hudson et al. 2004). Such a description needs to be included far beyond the ionization front.

The presence of free electrons in the gas with a fractional content exceeding 1 per cent impacts substantially on the ionization, excitation and dissociation rates because of energy loss by Coulomb collisions. As the fractional ionization increases the mean energy for ion couple increases as well, and eventually all the initial electron energy is converted into heat, with negligible residual inelastic rates.

¹ <http://physics.nist.gov/PhysRefData/Star/Text/ESTAR.html>

Finally, the total ionization rate is found by adding primary and secondary ionizations

$$\zeta_X = \zeta'_X + \left(1 + \sum_k Y_k \frac{\sigma_k^{(e)}}{\sigma_H}\right) \times (\zeta''_X + \zeta''_{X,C}), \quad (21)$$

where the sum includes only the contribution of heavy elements and $Y_k \sigma_k^{(e)}(E) = Y_{k0} \sigma_{k0}^{(e)}(E) + Y_{k+} \sigma_{k+}^{(e)}(E)$.

3 THE RÖNTGEN SPHERE

As first application of the formalism developed in the preceding sections, we revisit the concept of Röntgen sphere. According to Lorenzani & Palla (2001) these environments are defined as circumstellar regions in which the ionization rate due to X-rays exceeds the background level provided by cosmic rays, ζ_{cr} . Generally, in molecular clouds the ionization impact of cosmic rays is quantified by the number of H_2 ionization per second produced by cosmic-ray impacts. Such a quantity has been through the years observationally estimate to range from a few $10^{-18} s^{-1}$ to a few $10^{-16} s^{-1}$ in diffuse and dense interstellar clouds (Galli & Padovani 2015, and references therein). Here, we assume for the total cosmic-ray ionization rate the approximately median value $\zeta_{cr} = 1 \times 10^{-16} s^{-1}$ per hydrogen nucleus.

The size of the region is called Röntgen radius, R_X , and in the original formulation it is derived using the approximate relation

$$\zeta_{cr} = \frac{1.7 \bar{\sigma}}{\langle W \rangle} \int_{E_0}^{\infty} \mathcal{F}_X(E, R_X) \times (E/E_X)^{-n} dE, \quad (22)$$

where $\langle W \rangle = 0.035$ keV is a reasonable representative value for the mean energy for ion couple in a slightly ionized gas with solar abundances (see Dalgarno et al. 1999), $E_0 = 0.1$ keV, $E_X = 1$ keV, and the factor 1.7 accounts for the ionization due to secondary electrons. R_X is thus weakly dependent on the ratio between the X-ray luminosity defined as

$$L_X = \int_{E_0}^{\infty} \mathcal{L}_X(E) dE \quad (23)$$

and the cosmic-ray ionization rate ζ_{cr} , $R_X \propto \ln(L_X/\langle W \rangle \zeta_{cr})$, for $R_X \lesssim (1.7 \sigma_A(E_0)/4\pi \langle W \rangle \times L_X/\zeta_{cr})^{1/2}$. Thus, any increase of the cosmic-ray ionization rate, even above and beyond its characteristic figure in the cold neutral medium, $\zeta_{cr} = 1 \times 10^{-16} s^{-1}$, results in just a modest decrease in R_X .

R_X is weakly sensitive to the actual shape of the X-ray spectrum and directly dependent on the total X-ray luminosity. In the optically thin regime it does not vary with density, while decreases with increasing density otherwise. To simulate spectra differing significantly in shape, we adopt models for the thermal emission of hot plasmas with energies 0.3 (P03), 0.5 (P05) and 1 keV (P10) derived by Raymond & Smith (1977). These spectra are largely dominated by lines and oversampled with respect to the scope of this work. Thus, we bin them and derive the average number of photons in each bin. Defining the original spectrum as $s(E)$ (photons s^{-1}) and integrating it over the j -th energy bin of the set $\{\Delta E_k\}$, we get

$$S_j = \frac{1}{\Delta E_j} \int_{\Delta E_j} s(E) dE \quad \text{photons } s^{-1} \quad (24)$$

corresponding to the mean energy E_j (e.g. in eV) falling in the middle of ΔE_j . As consequence, the energies are related through the expression $E_{j+1} = E_j + (\Delta E_j + \Delta E_{j+1})/2$. In the following, we indicate the binned spectrum as $S(E)$. The X-ray spectral luminosity

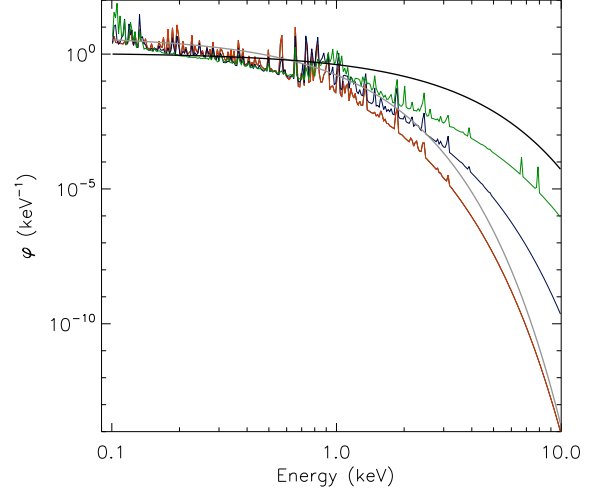


Figure 2. Spectral shapes as functions of the photon energy. Thermal plasma models: red (P03), blue (P05) and green (P10) lines. Thermal bremsstrahlung models: grey (B03) and black (B10) lines. For energies lower than ~ 0.1 keV all the fields are assumed to rapidly fade.

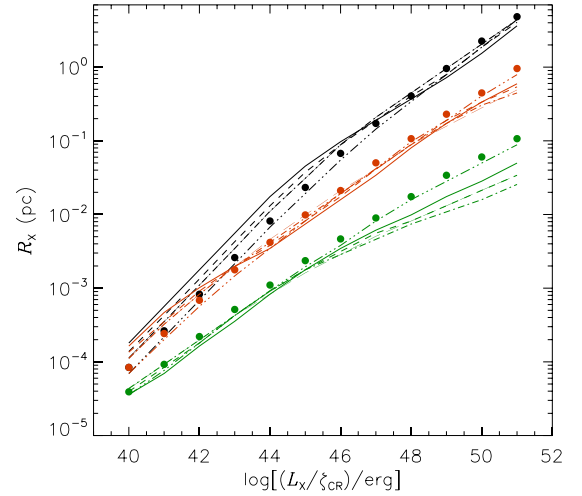


Figure 3. The Röntgen radius R_X as a function of the ratio of the X-ray luminosity L_X and the cosmic-ray ionization rate ζ_{cr} , for three values of the gas density $n_H = 10^2$ (black), 10^4 (red) and 10^6 cm^{-3} (green). For each density, we have used the spectral shapes described in Fig. 2: B03 (long dashed), B10 (dot-dot-dot-dashed), P03 (dot-dashed), P05 (short-dashed), and P10 (solid). Filled circles indicates values of the Röntgen radius obtained using the approximate relation derived by Lorenzani & Palla (2001), equation (22).

results

$$\mathcal{L}_X(E) = L_X \times \frac{S(E)}{\int_{\Delta E} S(E) dE} = L_X \times \varphi(E), \quad (25)$$

where $\varphi(E)$ is the spectral shape. For comparison with the original calculation by Lorenzani & Palla (2001), in the following we shall also consider thermal bremsstrahlung spectra at different plasma temperatures, 0.3 (B03) and 1 keV (B10). Spectral shapes are shown in Fig. 2 assuming single temperature thin thermal plasma models. All the fields are assumed to decrease sharply below $E_0 = 0.1$ keV (e.g. Nomura et al. 2007).

In Fig. 3, we show R_X as a function of the ratio L_X/ζ_{cr} , for some choice of the hydrogen number density. The Röntgen radius has

been derived through the use of the relation $\zeta_X(R_X) = \zeta_{\text{cr}}$, with ζ_X defined in equation (21). When $L_X/\zeta_{\text{cr}} \gtrsim 1 \times 10^{46}$ erg, R_X differs from that derived following the prescription of Lorenzani & Palla (2001), equation (22), by a factor around 2, corresponding to about one order of magnitude in volume. Increasing the gas density Röntgen radii decline roughly as $n_{\text{H}}^{1/2}$. Optical depth effects tend to remove rapidly the soft component of the spectrum as soon as $n_{\text{H}} \gtrsim 10^6 \text{ cm}^{-3}$. As a consequence the hardest spectral shapes (P10 and especially B10 models) produces more extended Röntgen radii than softer spectral profiles, although averaging over the volume ionization rates may results lower (see Section 6). Finally, in partially ionized regions R_X does not vary appreciably with the electron concentration n_e as long as the fractional ionization n_e/n_{H} lays below 1 per cent. For higher values, the degree of ionization falls rapidly as Coulomb dissipation dominates the energy loss of the secondary electron cascade.

4 IONIZATION STRUCTURE

Until now we considered X-rays impacting on a neutral gas. However, around hot stars the environment is also subjected to intense ultraviolet irradiation. We therefore extend our description of radiative transfer to include such spectral range.

Since the region is clearly overpressurized due to photoionization, an ionized nebula cannot exist in static equilibrium with its shape and density strongly dependent on the initial distribution of the circumstellar neutral gas. In many cases, the energetics is dominated by radiation fields with negligible mechanical energy conversion into radiation, and the size of the region is determined in all cases by the balance between ionizations and recombinations to the ground state of atomic hydrogen. However, the dynamical time-scales are much longer than those associated with microscopic processes, so that it is reasonable to assume the region as static. For the sake of simplicity, we also assume spherical envelopes in thermal and ionization equilibrium. This latter usually applies, although there may be cases in which departures from equilibrium are expected such as e.g. in the impact of ionization fronts on turbulent clouds (Tremblin et al. 2012). This occurs because of mixing of some ionized gas into the shadow of dense neutral gas in the transition zone.

Since the 1960s (e.g. Hummer & Seaton 1963), the ionized structure of circumstellar gas has been extensively studied. As usual we split the radiation field into two components, the attenuated direct stellar radiation and the diffuse component, and we exploit the so-called on-the-spot approximation in a dusty plasma, that consists in imposing that the hydrogen diffuse radiation field is locally absorbed only by hydrogen and dust and the helium radiation field only by helium and dust. This removes the transfer problem for diffuse radiation, and the ionization structure is thus determined by a single integration step, while the complete solution would require an iterative procedure. The equations of ionization equilibrium can be cast in a differential form for the column densities of neutral hydrogen, $j = 1$, and neutral, $j = 2$ and singly ionized helium, $j = 3$

$$\frac{1}{Y_j n_{\text{H}}} \frac{dN_j}{dr} = \frac{n_e K_j}{n_e R_j + \int_{m_j \mathcal{I}(0)}^{\infty} \sigma_j(E) [\mathcal{F}(E, r)/E] dE}, \quad (26)$$

where $Y_1 = 1$, $Y_2 = Y_3 = Y_{\text{He}}$, n_e is the electron number density, K_j the total recombination coefficient for the j -th species, $\mathcal{F}(E, r)$ the total radiation field including the diffuse component and $m_j = 1, 1.807$, and 4 for $j = 1, 2$, and 3, respectively. Using the notation

Table 2. Stellar properties.

Star type	Q_{H} (photons s^{-1})	T_* (K)	R_* (R_{\odot})	L_{bol} (L_{\odot})	M_* (M_{\odot})
B	1.3×10^{48}	30 500	7.47	2.0×10^4	15.8
O	8.9×10^{49}	47 000	17.2	5.0×10^5	39.8
WR	1.1×10^{49}	160 000	0.57	2.0×10^5	8.8

introduced in Section 2.2 equations (26) read as

$$\frac{dN_j}{dr} = \frac{Y_j n_{\text{H}}}{1 + (\zeta_j/K_j n_e)}, \quad (27)$$

where $\zeta_j = \zeta_{\text{UV}}^{(j)} + \zeta_X^{(j)}$ is the ionization rate per species j including both (extreme) ultraviolet and X-ray photoionization processes. Equations (27) are complemented by the closure relation for the number densities of charged species

$$n_e = n_{\text{H}^+} + n_{\text{He}^+} + 2n_{\text{He}^{2+}}. \quad (28)$$

Such equations are coupled through the optical depth, equation (9), extended to lower frequencies to include the ultraviolet portion of the spectrum.

The dust contribution to the optical depth in the ultraviolet range is computed by means of the cross-section

$$\sigma_{\text{d}}(\nu) = \frac{\delta_{\text{d}} R_V}{1.086} \frac{E_{B-V}}{N_{\text{H}}} \left(\frac{A_V}{A_V} \right) \sim 4.65 \times 10^{-4} \delta_{\text{d}} \left(\frac{A_V}{A_V} \right) \text{ Mb} \quad (29)$$

where δ_{d} is the depletion factor, $R_V = A_V/E_{B-V}$ the total to selective extinction, and E_{B-V} the colour excess related to the total hydrogen column density N_{H} through the gas-to-dust ratio $N_{\text{H}} = \mathcal{R}_{\text{gd}} \times E_{B-V}$. In the calculation, we used as fiducial value $\mathcal{R}_{\text{gd}} = 6.12 \times 10^{21} \text{ cm}^{-2} \text{ mag}^{-1}$ (Gudennavar et al. 2012) and we set $R_V = 3.1$; $\delta_{\text{d}} = 1$ corresponds to the average Galactic gas-to-dust mass ratio ~ 100 (e.g. Draine 2003). Dust extinction in the extreme ultraviolet cannot be measured directly. However, we can reasonably estimate dust attenuation by extrapolating the extinction in the far-ultraviolet (see the discussion in Tielens 2005). In our computed models, the visual extinction adds to $A_V \sim 1$ mag over the ionized region, corresponding to an optical thickness in the extreme ultraviolet of ~ 3 –4 (see e.g. Cecchi-Pestellini et al. 2010).

The coupled equations are integrated using standard techniques (i.e. the Bulirsch–Stoer method). At each radial integration step, we follow the time evolution of the number densities up to the steady state, solving a non-linear algebraic system for the three diffuse fields as in Tielens & de Jong (1979).

5 IONIZATION PROFILES AROUND MASSIVE STARS

We consider three representative massive stars (see Table 2), X-ray luminosities in the range $L_X = 10^{30}$ – 10^{35} erg s^{-1} , and three gas number densities, $n_{\text{H}} = 10^2, 10^4$ and 10^6 cm^{-3} in the circumstellar region. The ultraviolet field is approximated by a blackbody of temperature T_* , while X-ray fields have been described in Section 3. From now on, we shall exploit as reference the P05 spectral shape (see Fig. 2) unless otherwise stated. Each source is then characterized by three parameters, Q_{H} , the number of Lyman continuum photons per second emitted by the star, T_* , the radiation temperature and L_X the X-ray luminosity. We assume that without X-ray radiation the circumstellar region is ionization bounded. The labels O and B indicate two synthetic stars whose properties are reported in

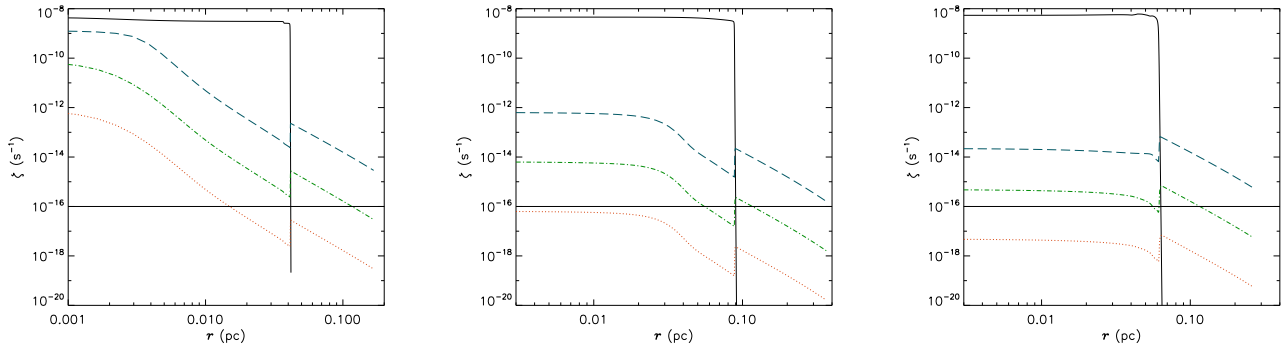


Figure 4. Photoionization rates as functions of the distance r from the ionizing source in a gas with number density $n_{\text{H}} = 10^4 \text{ cm}^{-3}$. Extreme ultraviolet: solid (black) line; X-rays: $L_{\text{X}} (\text{erg s}^{-1}) = 1 \times 10^{31}$, dotted (red) line, 1×10^{33} , dot-dashed (blue) lines, and 1×10^{35} , dashed (purple) lines. The thin black horizontal line indicates the level of the background cosmic-ray ionization rate $\zeta_{\text{cr}} = 1 \times 10^{-16} \text{ s}^{-1}$. Left-hand panel: B star; middle panel: O star; right-hand panel: WR star.

Mihalas & Binney (1981), that show approximately characteristics in between O3V and O5V (see e.g. the primary star of the system HD 150136) and B0V stellar types, respectively. The star labelled WR is WR93b, an oxygen sequence Wolf–Rayet star, spectral type WO3, discovered by Drew et al. (2004) in the Scutum–Crux arm of the inner Galaxy. This kind of stars constitute a final stage in massive star evolution, and should conclude their lives as Type Ic supernovae. The initial masses have been estimated to be in the range $40\text{--}60 M_{\odot}$ (Trumper et al. 2015). Since WR93b is a rather hot star, we include it in our sample to highlight the role of radiation temperature.

In all considered cases the ionization is initially dominated by the ultraviolet field with X-rays taking control in the proximity of the transition zone in which both H^+ and He^+ abundances fall sharply marking the onset of the photon-dominated region, the so-called Strömgren radius R_{S} (Osterbrock & Ferland 2006). When X-ray illumination is included, in the transition region the gas ionization does not follow the sharp fall of the ultraviolet ionization, declining much less steeply as X-rays propagate into the cloud volume creating a Röntgen region, whose extent is determined by the relative weights of the ultraviolet, X-ray and fast particle components. In the proximity of the Strömgren radius, where hydrogen recombines, the electron fraction drops abruptly, and the X-ray ionization increases in response to the closing of the Coulomb dissipation channel (Fig. 4). Thus, within the Strömgren region the photoelectron effect is the primary X-ray ionization source.

As it is clear from the results shown in Fig. 4 in some cases the Röntgen radius is not defined, being lower than the size of the Strömgren region. It is, however, worthwhile to recall that the Röntgen radius is not an absolute quantity, and it depends on the assumed level of the background cosmic-ray ionization rate.

In the case of O and WR stars for which H recombines before He, ionizations provided by X-rays inflate smoothly the ionized regions of hydrogen, helium and He^+ . In the B star case where the Strömgren radius of the hydrogen is greater than that of the helium, the extra-ionization source affects He only when hydrogen turns neutral. The net effect is a sharp increase of several orders of magnitude in the fractional abundances of He^+ and He^{2+} beyond the Strömgren radius (Fig. 5).

In Fig. 6, we plot R_{eq} the distance from the source for which the X-ray ionization rate matches the extreme ultraviolet one ($\sim R_{\text{S}}$) against the Röntgen radius, R_{X} , for a representative sample of models. In about two thirds of models the stars give origin to Röntgen regions,

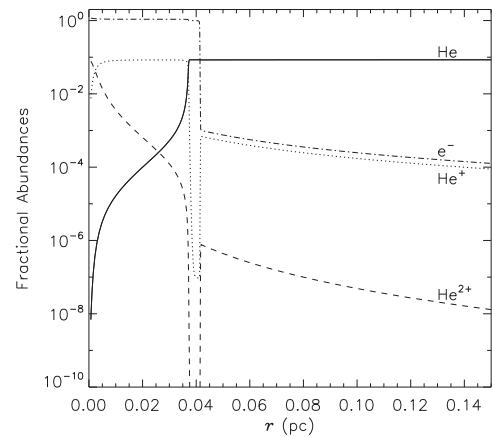


Figure 5. Fractional abundances of some members of the Helium family (and electrons) as functions of the distance r from the B star whose properties are reported in Table 2. The gas density is $n_{\text{H}} = 10^4 \text{ cm}^{-3}$ and the X-ray luminosity $L_{\text{X}} = 1 \times 10^{33} \text{ erg s}^{-1}$.

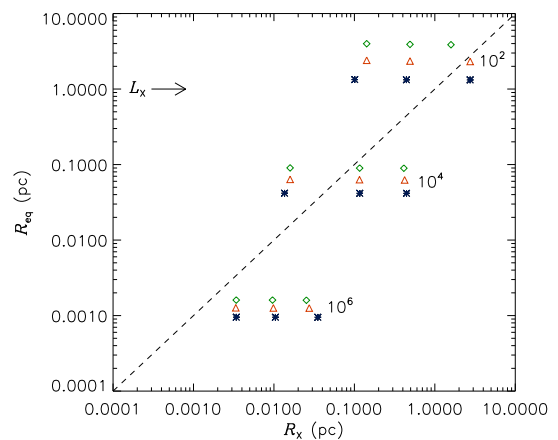


Figure 6. R_{eq} , the distance from the source for which the extreme ultraviolet and X-ray ionizations are the same, plotted versus the Röntgen radius, R_{X} , for B (blue *), O (green \diamond) and WR (red Δ) stars. Numerical labels indicate the gas number density in cm^{-3} ; the selected X-ray luminosities – increasing for each star in the direction of the arrow – are 1×10^{31} , 10^{33} and $10^{35} \text{ erg s}^{-1}$.

whose presence depends mainly on the density of the circumstellar medium. When $n_{\text{H}} = 10^2 \text{ cm}^{-3}$ only B and WR stars develop Röntgen regions at the highest X-ray luminosity. Increasing the circumstellar gas density, the number of successful models increase but the absolute values of R_{X} decrease. Such behaviour is a clear indication that the increase in the gas density impacts more effectively the extent of the H II region than R_{X} . These results upgrade the interpretation of Fig. 3 in the case of massive stars, as they show that in real cases although low densities induce large values of the Röntgen radius, R_{X} may be actually indefinite.

The volume averaged ionization rate $\langle \zeta_{\text{X}} \rangle$ increases with the gas number density for all kind of stars, and generally with increasing R_{X} (or $L_{\text{X}}/\zeta_{\text{cr}}$). For a gas with $n_{\text{H}} = 100 \text{ cm}^{-3}$, corresponding to the mean number density of a giant molecular cloud at 100 pc scale, there are no relevant effects beyond the Strömgren radius R_{S} . In embedding volumes with densities characteristic of clumps $n_{\text{H}} = 10^3\text{--}10^4 \text{ cm}^{-3}$, the volume averaged ionizations are approximately 10 times the background cosmic-ray ionization when $L_{\text{X}} \gtrsim 10^{35} \text{ erg s}^{-1}$. These effects occur on spatial ranges $R_{\text{X}} \sim 0.5 \text{ pc}$ ($R_{\text{X}}/R_{\text{S}} \sim 5\text{--}10$). Increasing further the gas densities within the range characteristic of dense cores the effects may be important, $\langle \zeta_{\text{X}} \rangle \gtrsim 100\zeta_{\text{cr}}$, but the size of the interested region is very small, few percent of parsec. Ultimately, the impact of X-rays on the environments of massive stars appears to be rather limited, with the exception of high-density regions, such as hot cores.

The above results have been derived using solar metallicities and average Galactic depletions. However, the ionization level depends on the metallicity and the depletion factor δ_{d} of the star embedding region. These two quantities are related, but for clarity we vary them independently. Their variations impact the results similarly but for different reasons: X-rays are principally absorbed by metals, while the depletion factor tunes the attenuation of the ultraviolet radiation. A decrease of a factor of 3 in metallicity heightens both the ionization and the extent of the Röntgen radius approximately one order of magnitude. Any increase in the depletion factor leads to higher dust extinctions, which decrease the density of the extreme ultraviolet radiation, resulting in an inward shift of the ionization front. As a consequence, X-rays take the control of the gas ionization with higher intensities than in the standard case.

The gathering of a large number of X-ray emitting massive stars might provide a significant contribution to the energetics of the embedding region. An interesting test case is given by the Cygnus OB2 association, one of our Galaxy's most massive star-forming regions. Its OB star members, whose number has been estimated to be ~ 200 (Wright, Drew & Mohr-Smith 2015) – see however the much larger value of ~ 2600 given in Knödseder (2000) – are known to be powerful X-ray emitters. Gredel, Black & Yan (2001) derived the lower limit of $Q_{\text{H}} = 7 \times 10^{50}$ ionizing photons s^{-1} , able to support a Strömgren sphere of $\sim 104 \text{ pc}$ at an electron density of $n_{\text{e}} = 34 \text{ cm}^{-3}$ (Downes & Rinehart 1966). Gredel et al. (2001) considered the possibility that strong stellar winds might have cleared out such a large region that the nebula is density-bounded, and thus leaking photons into the surrounding neutral gas, creating a Röntgen sphere. As noted by Drew et al. (2008) the lack of a bright H II region surrounding Cyg OB2 is possible if the clearing has occurred on time-scale greater than 5 Myr, consistently with the age distribution inferred from stellar evolutionary models (Wright et al. 2015). According to our calculations, the configuration needed to provide an X-ray ionization larger than the cosmic-ray level at 100 pc is a gas number density lower than $n_{\text{H}} = 20 \text{ cm}^{-3}$ and an aggregate X-ray luminosity of $3 \times 10^{38} \text{ erg s}^{-1}$, corresponding roughly to an average single star luminosity $\langle L_{\text{X}} \rangle \gtrsim 1 \times 10^{35} \text{ erg s}^{-1}$, depending on the number of

sources in the association. This value is larger than X-ray luminosities inferred for this region ranging between 10^{30} and $10^{31} \text{ erg s}^{-1}$ for intermediate-mass and low-mass stars, and between 2.5×10^{30} and $6.3 \times 10^{33} \text{ erg s}^{-1}$ for OB stars (Albacete-Colombo et al. 2007). This would support the possibility that the region was cleared out by stellar winds (e.g. Gredel et al. 2001) or other dynamical processes (see the discussion in Wright et al. 2015). The energy deposited by X-rays may be estimated through the relation

$$\mathcal{D}_{\text{X}} = 4\pi \int_0^{R_{\text{X}}} n_{\text{H}}(r) H_{\text{X}}(r) r^2 dr, \quad (30)$$

where

$$H_{\text{X}}(r) = \frac{L_{\text{X}}}{4\pi r^2} \int \sigma_{\text{T}}(E) \varphi(E) e^{-\tau(E,r)} dE \quad (31)$$

is the local X-ray energy deposition rate per particle (Maloney et al. 1996). Considering a cumulative X-ray luminosity $L_{\text{X}} = 3.9 \times 10^{34} \text{ erg s}^{-1}$ for the Cyg OB2 association (Flaccomio et al., in preparation) and a gas number density $n_{\text{H}} = 20 \text{ cm}^{-3}$, we find $R_{\text{X}} \sim 5 \text{ pc}$, and finally $\mathcal{D}_{\text{X}} \sim 2 \times 10^{34} \text{ erg s}^{-1}$. This value is approximately five orders of magnitude lower than the wind mechanical luminosity (i.e. the energy input rate to the wind bubble) for the Cygnus OB2 association $L_{\text{w}} = 1\text{--}2 \times 10^{39} \text{ erg s}^{-1}$ (e.g. Anchoadoqui et al. 2007). Interestingly, we have derived a similar value for the aggregate X-ray luminosity able to produce a Röntgen sphere with 100 pc radius.

6 PRE-MAIN-SEQUENCE STARS

In the previous section, we show that in circumstellar environments of massive stars, the gas ionization is dominated by the extreme ultraviolet fields. X-rays controls the ionization only beyond the edge of the H II region, if their residual flux is intense enough to overcome the background fast particle ionization rate. Such situation radically changes in the regions embedding PMS stars. These objects are particularly interesting in the context of this investigation because they are very active stars, they possess high $L_{\text{X}}/L_{\text{bol}}$ ratios, with low emission in the ultraviolet band. Furthermore, such stars show strong and frequent flaring activities. PMS stars exhibit X-ray luminosities significantly greater than those of main-sequence stars of the same spectral type. Moreover, being very young, they harbour discs and possibly young planets. Thus, their radiation environments may affect prebiotic evolution in the disc (e.g. Ciaravella et al. 2016; Jiménez-Escobar, et al. 2016), and possibly impact on biological processes (e.g. Smith, Scalo & Wheeler 2004).

We initially consider an isolated star representing a reasonable analogue of the PMS Sun, a 1.8 My old K0 T-tauri star of $1.08 M_{\odot}$, with both radius and bolometric luminosity approximately twice the solar ones (Preibisch et al. 1999). The star is located in Upper Scorpius. From the results of Fig. 3 relevant for the case of modest ultraviolet irradiation, selecting the ratio $L_{\text{X}}/\zeta_{\text{cr}} = 1 \times 10^{47} \text{ erg}$, and assuming a fractional ionization $n_{\text{e}}/n_{\text{H}}$ smaller than 1 per cent, we obtain $R_{\text{X}} = 0.19, 0.041$ and 0.006 pc for $n_{\text{H}} = 1 \times 10^2, 1 \times 10^4$ and $1 \times 10^6 \text{ cm}^{-3}$, respectively. Such values correspond to volume averaged ionization rates $\langle \zeta_{\text{X}} \rangle/\zeta_{\text{cr}} = 7.7, 15.3$ and 50.5 . Exploiting the harder P10 spectral shape, we now get $R_{\text{X}} = 0.19, 0.035$ and 0.006 pc for the assumed gas densities. In this case, the volume averaged ionization rates result $11.5, 29.8$ and 28.5 .

It is instructive to estimate how long a solar-like star maintains an appreciable Röntgen radius. Ribas et al. (2005) presented a selected sample of stellar proxies for the Sun with ages covering most of its main-sequence lifetime. Setting $n_{\text{H}} = 100 \text{ cm}^{-3}$ and normalizing to

Table 3. Röntgen radii for solar proxies.

Star ^a	Age (Gyr)	R_X^b (pc)	R_X^b (pc)	R_X^b (pc)
K0	0.002	1.9(-1) ^c	4.1(-2)	5.6(-3)
EK Dra	0.1	8.1(-2)	1.6(-2)	3.1(-3)
π^1 UMa + χ^1 Ori	0.3	3.7(-2)	8.3(-3)	1.8(-3)
κ^1 Cet	0.65	2.8(-2)	6.7(-3)	1.5(-3)
β Com	1.6	1.3(-2)	4.2(-3)	9.2(-4)
Sun	4.56	6.7(-3)	2.6(-3)	5.6(-4)
β Hyi	6.7	4.2(-3)	1.9(-3)	4.2(-4)
$\log_{10}(n_H/\text{cm}^{-3})$		2	4	6

Notes. ^aK0: Preibisch et al. (1999), all other stars: Ribas et al. (2005);

^b $L_X/\zeta_{\text{cr}} = 1 \times 10^{47}$ erg;

^c $1.9(-1) = 1.9 \times 10^{-1}$

the radius of a $1 M_\odot$ star (see Ribas et al. 2005), $R_X = 8 \times 10^{-2}$ pc at 0.1 Gyr and remains within a factor of 3 for a ten times older star. The Sun (4.56 Gyr old) produces a Röntgen radius 30 time lower than during its PMS. R_X values for seven representative stars (and age stages) are given in Table 3.

The value of the Röntgen radius derived for solar PMS proxy suggests that young stars formed in clusters may significantly contribute to the overall ionization level. Using the *COUP* correlation between X-ray luminosity L_X and the stellar mass (Preibisch et al. 2005), in combination with the model of star formation in ONC from Palla & Stahler (1999), Adams et al. (2012) derive the expectation value of the X-ray luminosity per star over the whole distribution of stellar masses (L_X) = 2.6×10^{30} erg s⁻¹. Such luminosity corresponding to a stellar mass of $\sim 1.2 M_\odot$, produces a Röntgen radius $R_X^0 = 0.13$ pc in a gas with $n_H = 1 \times 10^2$ cm⁻³, the mean number density for the Orion molecular cloud and a volume averaged X-ray ionization $\zeta_X^0 \sim 6 \times \zeta_{\text{cr}} = 6 \times 10^{-16}$ s⁻¹. Thus, the minimum number of PMS stars filling a cubic-parsec volume needed to provide an average ionization ζ_X^0 is $N_* \sim (1 \text{ pc}/R_X^0)^3 \sim 500$, a value consistent with, for example, Orion B, ρ Oph and Chamaeleon I, and much lower than the stellar density inferred for Orion A. The numbers of stellar members in the ONC extrapolated from the number of *COUP* sources at distances of 0.1 and 0.25 parsec from the cluster centre result 22 600 and 4 700 (King et al. 2012), respectively. The mean distance among the stars is then ~ 0.035 and 0.06 pc. At such distances the average ionizations increase to $\zeta_X^0 \sim 5 \times 10^{-14}$ and 1.3×10^{-14} s⁻¹, respectively. Such widespread diffuse X-ray radiation must be taken into account in the ionization balance.

High X-ray ionization background levels are excluded from regions of much lower stellar density, such as L1495 in Taurus, in which (at most) 10 stars per cubic parsec, are inferred for a distance of approximately 1 pc from the cluster centre.

7 CONCLUSIONS

In this work, we present a detailed model of the interaction of stellar X-rays with circumstellar matter. We test and validate this model studying the formation of regions in which X-rays are the major ionization channel. Such regions, called Röntgen spheres (Lorenzani & Palla 2001) may have considerable importance in the chemical and physical evolution of the gas embedding the emitting star.

For PMS stars, generally characterized by modest ultraviolet irradiation and appreciable L_X/L_{bol} ratios, we find that significant volumes of gas are affected by ionization levels exceeding largely the cosmic-ray background ionization. In clusters arising in regions

of vigorous star formation X-rays create an ionization network pervading densely the interstellar medium. Such X-ray background radiation in young embedded clusters is potentially a key factor in star and planet formation (e.g. Feigelson 2010), providing a natural feedback mechanism that may act, for example, as a brake to accelerating star formation, through an increase of the coupling of the magnetic field to the cloud material via ambipolar diffusion (Lorenzani & Palla 2001). Whatever the case may be, doubtless X-rays are an important component of the energy balance and in the chemical evolution.

In regions of massive star formation the radiative transfer feedback appear to be of limited use. The formation of extended volumes with relevant levels of ionization is efficient just in a narrow range of gas volume densities, and only for very high X-ray luminosity and L_X/L_{bol} ratios. In the case of Cygnus OB2 association, the cumulative extent of the Röntgen spheres suggests that mechanical energy injection from fast stellar winds (and possibly supernovae, see Wright et al. 2015) played a major role in dispersing dense dusty gas and possibly in driving outflows from the region. Preliminary studies of the energetics of the Tarantula Nebula (30 Doradus) in the Large Magellanic Cloud give support to this interpretation, suggesting that the total kinetic energy of the nebula is dominated by the turbulent and bulk motions of H II gas (Wang & Lim 2016). This is particularly interesting as the Large Magellanic Cloud is a metal-poor galaxy, in which X-rays should be more pervasive than in typical Galactic regions.

In conclusion, our study provides an accurate estimate of the degree of ionization in regions embedding X-ray emitting stars, and quantify the X-ray contribution to the total ionization of the gas. This work is not only a presentation of the basic processes to be considered, but it supports the idea that X-ray could be among the most relevant ingredients in the evolution of a variety of astronomical regions.

ACKNOWLEDGEMENTS

We acknowledge the inspiration of the pioneering work by A. Lorenzani and F. Palla (2001), who first addressed the problem from this perspective. We are grateful to M. Guarcello and E. Flaccomio for sharing information about Cyg OB2 association and ONC.

The authors acknowledge the support of the Agreement ASI-INAF n.2015-038-R.1 ‘Ariel - Assessment phase’.

We would also like to thank the anonymous reviewer for her/his suggestions, which significantly contributed to improving the clarity of the paper.

REFERENCES

- Adamkovic M., Glassgold A. E., Meijerink R., 2012, ApJ, 736, 143
 Adams F. C., Fatuzzo M., Holden L., 2012, PASP, 124, 913
 Albacete-Colombo J. F., Flaccomio E., Micela G., Sciortino S., Damiani F., 2007, A&A, 464, 211
 Anchordoqui L. A., Beacom J. F., Goldberg H., Palomares-Ruiz S., Weiler T. J., 2007, Phys. Rev D, 75, 063001
 Asplund M., Grevesse N., Sauval J., Scott P., 2009, ARA&A, 47, 481
 Bahcall J. N., Bahcall N. A., Kozlovsky B.-Z., 1971, A&A, 13, 1
 Bartlett P. L., Stelbovics A. T., 2004, At. Data Nucl. Data Tables, 86, 235
 Bradford C. M. et al., 2011, ApJ, 741, L37
 Cecchi-Pestellini C., Ciaravella A., Micela G., 2006, A&A, 458, L13
 Cecchi-Pestellini C., Cacciola A., Iatì M. A., Saija R., Borghese F., Denti P., Giusto A., Williams D. A., 2010, MNRAS, 408, 535
 Ciaravella A., Chen Y.-J., Cecchi-Pestellini C., Jiménez-Escobar A., Muñoz-Caro G. M., Juang K.-J., Huang C.-H., 2016, ApJ, 819, 38

- Cravens T. E., Victor G. A., Dalgarno A., 1975, *Planet. Space Sci.*, 23, 1059
- Dale J. E., Bonnell I., 2011, *MNRAS*, 414, 321
- Dalgarno A., Yan M., Liu W., 1999, *ApJS*, 125, 237
- Downes D., Rinehart R., 1966, *ApJ*, 144, 937
- Draine B. T., 2003, *ARA&A*, 41, 241
- Drew J. E., Barlow M. J., Unruh Y. C., Parker Q. A., Wesson R., Pierce M. J., Masheder M. R. W., Phillips S., 2004, *MNRAS*, 351, 206
- Drew J. E., Greimel R., Irwin M. J., Sale S. E., 2008, *MNRAS*, 386, 1761
- Fatuzzo M., Adams F. C., 2008, *ApJ*, 675, 1361
- Favata F., Flaccomio E., Reale F., Micela G., Sciortino S., Shang H., Stassun K. G., Feigelson E. D., 2005, *ApJS*, 160, 469
- Feigelson E. D., 2010, *Publ. Natl. Acad. Sci.*, 107, 7153
- Galli D., Padovani M., 2015, preprint ([arXiv:1502.03380](https://arxiv.org/abs/1502.03380))
- Getman K. V., Flaccomio E., Broos P. S. et al., 2005 *ApJS*, 160, 319
- Giacconi R., Murray S., Gursky H., Kellogg E., Schreier E., Tananbaum H., 1972, *ApJ*, 178, 281
- Gredel R., Black J. H., Yan M., 2001, *A&A*, 375, 553
- Gudennavar S. B., Bubbly S. G., Preethi K., Murthy J., 2012, *ApJS*, 199, 8
- Hamaguchi K., Corcoran M. F., Russell C. M. P. et al., 2014, *ApJ*, 784, 125
- Holden L., Landis E., Spitzig J., Adams F. C., 2011, *PASP*, 123, 14
- Hollenbach D., Gorti U., 2009, *ApJ*, 703, 1203
- Hudson J. E., Vallance C., Harland P. W., 2004, *JPhB*, 37, 445
- Hummer D. G., Seaton M. J., 1963, *MNRAS*, 125, 437
- Jackson J. D., 1975, *Classical Electrodynamics*. Wiley, New York
- Jiménez-Escobar A., Chen Y.-J., Ciaravella A., Huang C.-H., Micela G., Cecchi-Pestellini C., 2016, *ApJ*, 820, 25
- King R. R., Parker R. J., Patience J., Goodwin S. P., 2012, *MNRAS*, 421, 2025
- Knödlseder J., 2000, *A&A*, 360, 539
- Lorenzani A., Palla F., 2001, in *From Darkness to Light*, ASP Conf. Ser. Vol. 243, Montemerle T., André Ph. eds., Astron. Soc. Pac., San Francisco, p. 745
- Maloney P. R., Hollenbach D. J., Tielens A. G. G. M., 1996, *ApJ*, 466, 561
- Micela G., 2002, in Montesinos B., Gimenez A., Guinan E.F., eds., ASP Conf. Ser. Vol. 269, *The evolving Sun and Its Influence on Planetary Environments*, Astron. Soc. Pac., San Francisco, p. 107
- Mihalas D., Binney J., 1981, *Galactic Astronomy*. W.H. Freeman and Company
- Morita M., Yabushita S., 2008, *J. Comp. Chem.*, 29, 2471
- Nomura H., Aikawa Y., Tsujimoto M., Nakagawa Y., Millar T. J., 2007, *ApJ*, 661, 334
- Osterbrock D. E., Ferland G. J., 2006, *Astrophysics of Gaseous Nebulae and Active Galactic Nuclei*. Univ. Science Books, Sausalito
- Palla F., Stahler S. W., 1999, *ApJ*, 525, 772
- Preibisch T., Zinnecker H., 1999, *AJ*, 117, 2381
- Preibisch T., Kim Y.-C., Favata F. et al., 2005, *ApJS*, 160, 401
- Raymond J. C., Smith B. W., 1977, *ApJS*, 35, 419
- Ribas I., Guinan E. F., Gudel M., Audard M., 2005, *ApJ*, 622, 680
- Rybicki G., Lightman A. P., 2004, *Radiative Processes in Astrophysics*. Wiley-Interscience, New York
- Samson J. A. R., Haddad G. N., 1994, *JOSA B*, 11, 277
- Smith D. S., Scalo J., Wheeler J. C., 2004, *OLEB*, 34, 51
- Tarawa H., Kato T., 1987, *At. Data Nucl. Data Tables*, 36, 167
- Tielens A. G. G. M., 2007, *The Physics and The Chemistry of the Interstellar Medium*. Cambridge Univ. Press, Cambridge
- Tielens A.G.G.M., de Jong., T 1979, *A&A*, 75, 326
- Tiné S., Lepp S., Gredel R., Dalgarno A., 1997, *ApJ*, 481, 282
- Tremblin P., Audit E., Minier V, Schmidt W., Schneider N., 2012 *A&A*, 546, A33
- Trumper P., Straal S. M., Sanyal D., Sana H., de Koter A., Gräfener G., Langer N., Vink J. S., de Mink S. E., Kaper L., 2015, *A&A*, 581, A110
- Turter C. B., Salpeter E. E., 1969, *ApJ*, 156, 953
- Turter C. B., Tucker W. H., Salpeter E. E., 1969, *ApJ*, 156, 943
- Verner D. A., Yakovlev D. G., 1995, *A&AS*, 109, 125
- Wang Q.-D., Lim S., 2016, *AAS*, 227, 323
- Williams D. A., Viti S., 2014, *Observational Molecular Astronomy: Exploring the Universe Using Molecular Line Emissions*. Cambridge Univ. Press, Cambridge
- Wright N. J., Drew J. E., Mohr-Smith M., 2015, *MNRAS*, 449, 741
- Yan M., Sadeghpour H. R., Dalgarno A., 1998, *ApJ*, 496, 1044

This paper has been typeset from a $\text{\TeX}/\text{\LaTeX}$ file prepared by the author.